


Eccentricity fault detection in brushless doubly fed induction machines

Mojtaba Afshar¹  | Salman Abdi² | Ashknaz Oraee³ | Mohammad Ebrahimi⁴ | Richard McMahon⁵

¹Electrical Engineering Department, The University of Texas at Dallas, Dallas, TX, USA

²School of Engineering, University of East Anglia, Norwich, UK

³Engineering Department, Cambridge University, Cambridge, UK

⁴Department of Electrical and Computer Engineering, Isfahan University of Technology, Isfahan, IRAN

⁵Power Electronics and Electrical Machines Department, WMG, Coventry, UK

Correspondence

Mojtaba Afshar, Electrical Engineering Department, The University of Texas at Dallas, TX, USA.
Email: mojtaba.afshar@utdallas.edu

Abstract

A new fault diagnosis method for detecting the rotor eccentricity faults including static, dynamic and mixed eccentricity is proposed for brushless doubly-fed induction machines (BDFIMs). BDFIMs are attractive alternatives for the conventional doubly-fed induction generator (DFIG) for offshore wind power generation; therefore, paying attention to their fault detection is essential. Existing fault detection methods for conventional induction machines cannot be directly applied to the BDFIM due to its special rotor structure and stator winding configurations as well as complex magnetic field patterns. This article proposes a novel fault detection method based on motor current signal analysis to determine stator current harmonics, induced by the nested-loop rotor slot harmonics (NRSs), as fault indices. The analysis is performed under healthy conditions and with different types of rotor eccentricity. Finally, a sensitivity analysis is carried out to confirm the practicability of the proposed technique with various fault intensities and load conditions. Analytical winding function approach, finite element analysis and experimental tests on a prototype D180 BDFIM are used in this study to validate the proposed fault detection technique.

1 | INTRODUCTION

The brushless doubly-fed induction machine (BDFIM) is an alternative to the well-established doubly-fed induction generator (DFIG) for use in wind turbines since it offers improved reliability and reduced capital and maintenance costs [1]. It retains the low-cost advantage of the DFIG system as it only requires a fractionally rated converter and does not use permanent magnet materials. In addition, the machine has no brushed contact to the rotor, eliminating a common source of failures and therefore making it a particularly attractive machine for offshore wind turbines. Furthermore, the BDFIM is intrinsically a medium-speed machine, enabling the use of a simplified one or two stage gearbox. A schematic of the BDFIM grid connection is shown in Figure 1.

The BDFIM has its origins in the self-cascaded machine and has two non-coupling stator windings with different pole number, known as power winding (PW) and control winding (CW). A specially designed rotor called nested-loop rotor used to create indirect cross-coupling between stator winding magnetic fields [2]. Other applications have also been

considered for the BDFIM, such as stand-alone generator for off-grid applications [3], drive in pump applications [4] and ship shaft generator systems [5].

The design of the BDFIM is not straightforward since there are more variables to consider than the conventional induction machines [6]. Attention has been given to some design aspects of the BDFIM used in adjustable speed applications reported in [7–9]. Also, several large BDFIMs have been reported including the 75-kW machine [10], the 200-kW machine [11] and the 250-kW machine [12]. The latter, believed to be the largest to date, was conceived as a steppingstone towards commercial MW scale BDFIMs. In a wind turbine application, the machine is matched to the rest of the drive train so the natural speed, dependent on the sum of the pole-pairs, and the speed range around natural speed, typically $\pm 30\%$, are of interest.

Rotor eccentricity faults are amongst the most frequent faults in electrical machines taking between 50% and 60% of mechanical faults [13, 14]. An eccentric rotor motion occurs when the rotor axis is not aligned with the axis of the stator bore. The effects of rotor eccentricity in various electrical

This is an open access article under the terms of the Creative Commons Attribution License, which permits use, distribution and reproduction in any medium, provided the original work is properly cited.

© 2021 The Authors. *IET Electric Power Applications* published by John Wiley & Sons Ltd on behalf of The Institution of Engineering and Technology.

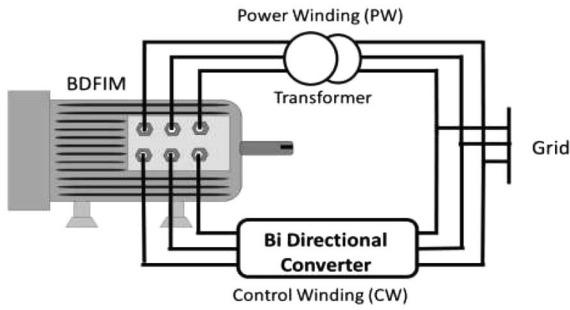


FIGURE 1 Schematic of the BDFIM grid connection

machine performance such as induction machines [15], and permanent magnet synchronous machines [16], have been studied and different fault detection methods have been proposed. For BDFIM, a method based on motor current signal analysis (MCSA) has been introduced in [17, 18] to detect inter-turn short circuit fault using FFT analysis and wavelet transform, respectively. In addition, an MCSA-based method also has been presented in [19] to detect static eccentricity (SE) fault in BDFIM. However, other types of rotor eccentricity including dynamic eccentricity (DE) and mixed eccentricity (ME) have not been studied yet.

The BDFIMs magnetic field has two principal components with different pole numbers, and the interaction of these two components leads to more complex vibration patterns than those in the induction machine [20]. The presence of rotor eccentricity further modulates the field patterns, exacerbating the resulting vibration. Rotor whirling caused by the rotor eccentricity generates an electromagnetic force also known as the unbalanced magnetic pull (UMP) that acts between the rotor and stator.

This force can be decomposed into two components: the radial force, acting in the direction of the shortest airgap; and the tangential force, which is perpendicular to the radial force. The amplitude and direction of the latter force depend on the operating conditions of the machine, rotor whirling frequency and rotor radius [21]. Acting in the direction of the shortest airgap, UMP tends to further increase the eccentricity magnitude and may cause serious damage to the machine or the entire drive. In addition, UMP acts as a major source of vibration and the acoustic noise.

The effects of rotor eccentricity on the BDFIM stator back iron deflection have been studied in [22], and a special stator parallel winding design has been proposed to suppress the resulting deflection. In [23] an experimental work was carried out on a prototype BDFIM to measure the vibration and noise at different rotor speeds in synchronous mode of operation. Various sources of vibration including airgap non-uniformity have been identified in the machine. However, no generic method was proposed in the above works to detect rotor eccentricity faults in the BDFIM.

Signal-based methods have been widely used for detecting faults in electrical machines because of their simplicity, real-time diagnosis and rapid response. Amongst them MCSA, based on the analysis of electrical current waveforms, is a

popular fault diagnosis method that has been widely used in electrical machines fault detection [24, 25].

A novel analytical method is proposed for the BDFIM to determine time harmonic frequencies induced in stator winding currents by the nested-loop rotor slot harmonics (NRSBs) when the rotor is centric and different types of rotor eccentricity are presented. Then, the signature harmonic frequencies induced in the stator currents are identified for each eccentricity type and used as fault indices. The proposed method is validated using an analytical winding function approach and finite element (FE) analysis for a D180 BDFIM operating in synchronous mode under rotor centric and eccentric conditions. Finally, a sensitivity analysis is performed in order to investigate the practicality of the proposed technique for detecting eccentricity faults under various fault intensities.

2 | BRUSHLESS DOUBLY-FED INDUCTION MACHINE

2.1 | BDFIM operation

The BDFIM consists of two sets of three-phase windings with different pole-pair numbers wound on a common stator frame. The machine's winding connections to the supply is shown in Figure 1. The BDFIM can operate under three different modes, induction, cascaded and synchronous, the latter is the main mode of operation where the PW is connected to the grid via an auto transformer and the CW is supplied with a fractionally rated power converter. The pole numbers are chosen to avoid direct coupling between PW and CW and the coupling is enabled by a special rotor design called nested-loop rotor. The number of rotor nests, N_n , is determined in a way that the rotor can couple both stator magnetic fields [2]:

$$N_n = p_p + p_c \quad (1)$$

where p_p and p_c are power and control winding pole-pair numbers, respectively.

The BDFIM normally operates in the synchronous mode in which the shaft speed is independent of the torque exerted on the machine, as long as it is smaller than the pull-out torque. The rotor angular speed ω_r , determined by the frequencies and pole-pair numbers of the stator windings, is given by:

$$\omega_r = \frac{\omega_p + \omega_c}{p_p + p_c} \quad (2)$$

where ω_p and ω_c are angular supply frequencies of PW and CW, respectively.

2.2 | Prototype D180 BDFIM

Table 1 gives specifications of the D180 prototype BDFIM used in this study. The rotor is of a nested-loop design

Parameter	Value	Parameter	Value Heading
Stack length	190 mm	Airgap length	0.9 mm
PW winding type	Dist. Double layer	PW no. of turns	160
CW winding type	Dist. Double layer	CW no. of turns	160
PW no. of poles	4	PW rated voltage	240 V at 50 Hz
CW no. of poles	8	CW rated voltage	172 V at 25 Hz
PW resistance	6.3 Ω	PW leakage ind.	3.8 mH
CW resistance	3.9 Ω	CW leakage ind.	9 mH
Rotor type	Nested loop	Rotor no. of slots	36
Nests no.	6	Rated power	7.8 kW at 750
Rotor resistance	Inner: 104 $\mu\Omega$	Middle: 119 $\mu\Omega$	Outer: 134 $\mu\Omega$
Rated torque	100 Nm	Efficiency	>92%

TABLE 1 Specifications for the D180 BDFIM

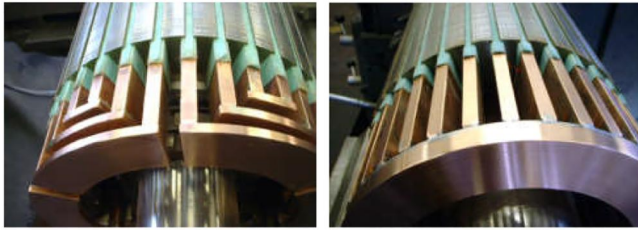


FIGURE 2 Experimental nested-loop rotor configuration

consisting of 36 slots. As it has $p_p = 2$ and $p_c = 4$, the rotor has $N_n = 6$ nests terminated with a common end ring at one end only. Each nest is allocated six slots. Therefore, three concentric loops are housed within each nest. Figure 2 shows the experimental nested-loop rotor configuration. The stator windings are composed of several coils connected in series to form each winding phase. The delta connected power winding is connected to the grid through a variac and is supplied with 204 Vrms, 50 Hz under normal conditions. The control winding is also connected in delta and supplied by a unidirectional converter. Additionally, a sinusoidal filter is connected between the converter output and the control winding to eliminate components related to the converter's switching frequency. The PW and CW winding configurations were presented and discussed in [2]. The prototype BDFIM is coupled to a DC machine equipped with a commercial DC drive. An incremental encoder with 10,000 pulse per revolution is used to measure the shaft rotational speed. The voltages and currents of each stator phase are measured by LEM LV 25-p and LEM LTA 100-p transducers, respectively. The speedgoat control system described in [23] is used to control the machine operation and log output results used for further analysis.

2.3 | Winding function method

Winding function method is based on the coupled magnetic circuit theory and is used to calculate stator winding

inductances by means of the magnetic energy stored in the airgap under both healthy and faulty conditions. Based on [15], the mutual inductance between the coils A and B , L_{AB} , can be calculated as:

$$L_{AB} = \mu_0 r l \int_0^{2\pi} n_A(\varphi, \theta_r) N_B(\varphi, \theta_r) g^{-1}(\varphi, \theta_r) d\varphi \quad (3)$$

where n_A is turn function for coil A and N_B is winding function for coil B . Also, μ_0 is permeability of air, l and r are the machine's stack length and rotor diameter, respectively. The inverse of rotor airgap function can be expressed as:

$$g_e(\varphi, \theta_r) = g_0(1 - e_s \cos(\varphi) - e_d \cos(\varphi - \theta_r)) \quad (4)$$

where φ shows the position along the stator inner surface and e_s and e_d are the degrees of static and dynamic eccentricity, respectively.

A winding function model has been developed for the D180 BDFIM, using which all the PW and CW inductances can be calculated under healthy and rotor eccentricity conditions. Having obtained the PW and CW inductances and by using the machine's coupled circuit model followed by performing a series of transformations [2], the stator PW and CW currents can be obtained in different operating conditions.

2.4 | Finite element model development

The D180 BDFIM has been modelled in a synchronous mode and at full load using the ANSYS Maxwell FE software. The model was solved as a voltage-fed problem so that simulation results can be compared directly to experimental measurements. A 2D FE analysis was performed to reduce the computational time by assuming that the effects of the axial flux are negligible. The end region leakage effects were incorporated into the analysis using lumped parameters. The modelling was performed using the time-stepping method for

accurate analysis and consideration of non-linear properties of the iron circuit. The operating conditions are shown in Table 2. In the synchronous mode of operation, the PW is connected directly to the grid and the CW is supplied with variable voltage at variable frequency from a converter. The implementation of BDFIM synchronous operation in FE is particularly challenging because the CW excitation voltage required to set a specific load condition which cannot be predetermined as the machine is not stable in the open loop. Therefore, a closed-loop controller was implemented with details described in [21]. Figure 3 shows the magnetic flux distribution of the machine under synchronous mode of operation. Search coils were fitted into the BDFIM to measure the flux densities in a stator tooth and the back iron, as shown in Figure 4. The measured and predicted flux densities in stator tooth and back iron are illustrated in Figure 5. The close agreement between FE results and the experimental results confirms validity of FE models.

3 | MCSA FAULT DETECTION METHOD

A new MCSA-based method is proposed to detect eccentricity faults in BDFIMs. The BDFIM airgap magnetic field is analytically obtained for the case of centric rotor as well as different types of rotor eccentricity and the NRSBs are

TABLE 2 Operating conditions for simulations and experiments

Parameter	Value	Parameter	Value Heading
Torque	103 Nm	Speed	750 rpm
V_{pw}	204 V at 50 Hz	PW frequency f_{pw}	50 Hz
V_{cw}	50 V at 4 Hz	CW frequency f_{cw}	4 Hz
Slip S_p	0.64		

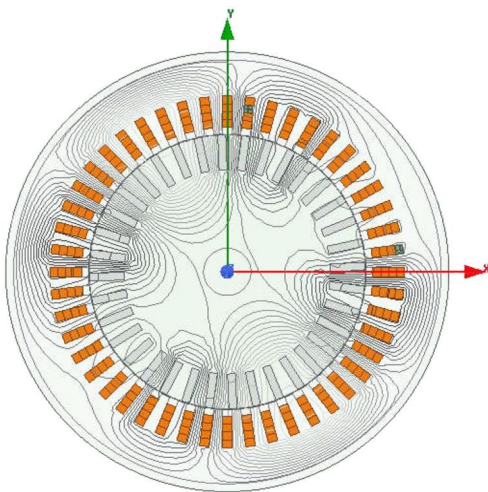


FIGURE 3 Magnetic flux distribution of the BDFIM in the synchronous mode of operation

determined. The analytical derivations of time harmonic frequencies induced in the stator current due to NRSB are then presented and the signature frequencies associated to each eccentricity fault are identified. These frequencies are used as fault indices for diagnosis of the eccentricity faults in the BDFIM.

The proposed fault detection technique can be applied to both PW and CW currents. However, although there is no restriction in using CW current, it will be shown in the following sections that the analysis of PW current will suffice for the detection of all different eccentricity types in the BDFIM. Therefore, only PW current is considered in the proposed MCSA technique.

It should be noted that, the signature frequencies when PW current is analysed will differ from those when CW current is considered. Therefore, the signature frequencies must be explicitly determined for each of the above cases.

3.1 | Healthy condition

There is always a degree of space harmonic contents in the airgap magnetic field generated due to the finite number of stator slots. The magnetic field of a distributed stator winding supplied by a pure sinusoidal voltage can be expressed as [26]:

$$F_{Hp}(t, \theta_s) = \widehat{F}_{Hp} \cos(\omega_p t - H_p \theta_s) \quad (5)$$

$$H_p = (1 \pm 6g)p_p \quad \forall g = 0, 1, 2, \dots$$

where F_{Hp} is the PW space harmonic order corresponding to H -th harmonic, H_p is the order of PW space harmonic, ω_p is the PW angular frequency, and θ_s is angular position in the stator reference frame. The fundamental component of PW MMF, F_p , in the stator reference frame can be obtained from Equation (5) when g is zero:

$$F_p(t, \theta_s) = \widehat{F}_p \cos(\omega_p t - p_p \theta_s) \quad (6)$$

Under healthy conditions, the airgap permeance function without considering saturation and slot effects is expressed by:

$$P \approx P_0 \quad (7)$$

By multiplying Equations (6) and (7) the PW airgap flux, ϕ_p , in the stator reference frame is written as:

$$\phi_p(t, \theta_s) = \widehat{F}_p P_0 \cos(\omega_p t - p_p \theta_s) \quad (8)$$

The PW airgap flux in the rotor reference frame, can be calculated by substituting $\theta_s = \theta_r + \omega_r t$ in Equation (8).

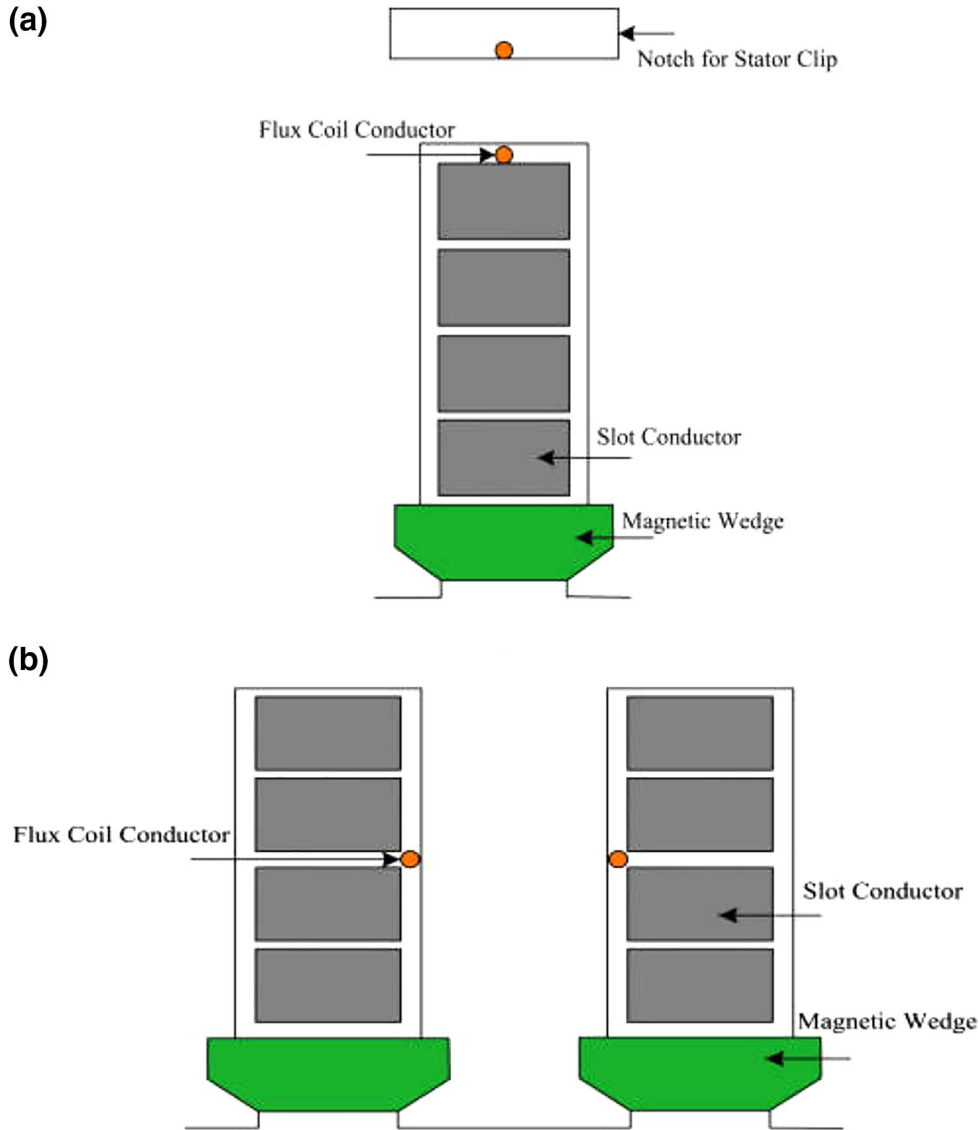


FIGURE 4 Search coils' position in the D180 BDFIM (a) stator back iron (b) stator teeth

$$\phi_p(t, \theta_r) = \widehat{F}_p P_0 \cos\left((\omega_p - p_p \omega_r)t - p_p \theta_r\right) \quad (9)$$

where θ_r is angular position in the rotor reference frame. According to the Faraday's Law, the induced voltage in rotor bars can be calculated by:

$$e_{rp}(t, \theta_r) = N_t \frac{d\phi_p}{dt} \quad (10)$$

where N_t is rotor turn function and is obtained from Fourier series of the rotor winding distribution as presented in [27]. The induced voltage generates electrical current in rotor bars. Hence, rotor electrical currents produce MMF in the airgap, which can be calculated by multiplying the current and the turn function of the rotor. The nested-loop rotor MMF in rotor reference frame is then:

$$F_{rp}(t, \theta_r) = \widehat{F}_{rp}(\omega_r) P_0 \sin\left(\begin{array}{l} (\omega_p - p_p \omega_r)t - \\ (p_p \pm kN_n)\theta_r \end{array}\right) \quad (11)$$

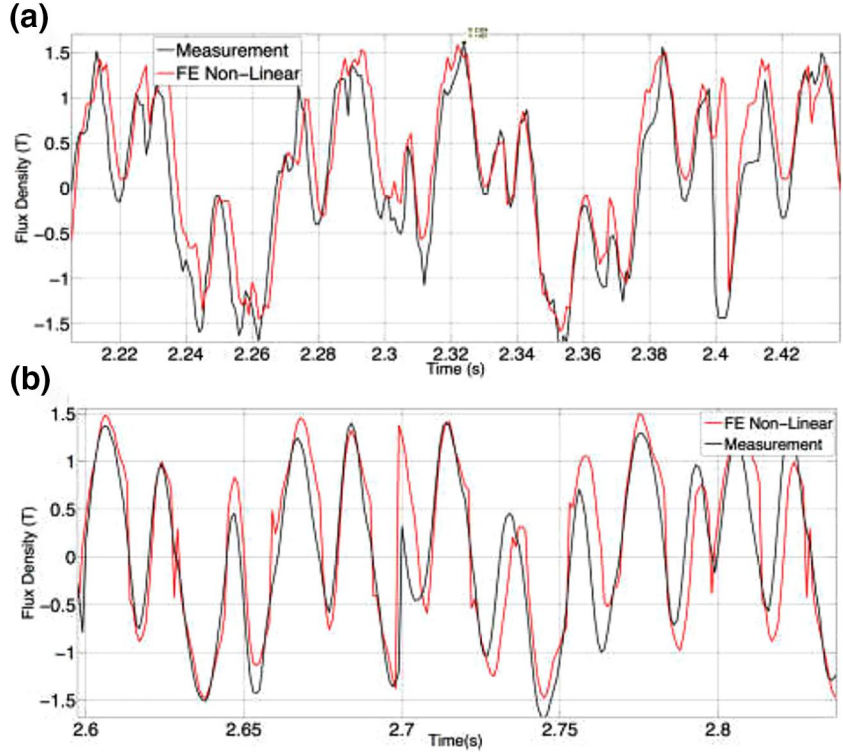
According to Equation (11), the nested-loop rotor generates MMF with $(p_p \pm kN_n)$ harmonic orders in rotor reference frame where $k = 0, 1, 2, \dots$. Using Equations (5) and (9), and $\theta_r = \theta_s - \omega_r t$, the rotor airgap flux in the stator reference frame can be calculated as:

$$\phi_{rp}(t, \theta_s) = \widehat{F}_{rp}(\omega_r) P_0^2 \sin\left(\begin{array}{l} (\omega_p \pm kN_n \omega_r)t - \\ (p_p \pm kN_n)\theta_s \end{array}\right) \quad (12)$$

The PW slip (s_p) is defined as:

$$s_p = \frac{\omega_p - p_p \omega_r}{\omega_p} \quad (13)$$

FIGURE 5 Predicted and measured flux density in D180 BDFIM (a) stator back iron (b) stator teeth



By substituting ω_r from Equation (13) in Equation (12), the rotor airgap flux can be expressed as:

$$\phi_{rp}(t, \theta_s) = \widehat{F}_{rp}(\omega_r) P_0^2 \sin \left(\begin{array}{l} \left(1 \pm \frac{kN_n}{p_p} (1 - S_p) \right) \omega_p t \\ - (p_p \pm kN_n) \theta_s \end{array} \right) \quad (14)$$

According to Equation (14), the rotor airgap flux consists of NRSH components, which induce time harmonics in the PW. These time harmonics can be obtained from:

$$\left\{ \begin{array}{l} f_{H(k)} = \left(1 + k \frac{N_n}{p_p} (1 - S_p) \right) f_p \\ \forall |p_p + kN_n| \in |H_p| \\ f_{H(k)} = \left(1 - k \frac{N_n}{p_p} (1 - S_p) \right) f_p \\ \forall |p_p - kN_n| \in |H_p| \end{array} \right. , \quad k = 0, 1, 2, \dots \quad (15)$$

where $f_{H(k)}$ is the k -th component frequency in the PW current spectrum under healthy condition and f_p is the PW supply voltage frequency. The $f_{H(k)}$ frequencies for the values of k satisfying $|p_p \pm kN_n| \in |H_p|$ can hence be seen in the PW current spectrum. The same analytical derivation described above will also be used in the following sections for different rotor eccentricity types in order to obtain the induced time harmonic frequencies in the PW current as fault indices.

3.2 | Rotor eccentricity fault condition

In electrical machines the large radial forces acting on the surface of the rotor cancel each other out when the rotor axis is aligned with the stator axis [21]. Similarly, tangential forces are balanced such that only an axially rotating momentum is produced. If the rotor is eccentric, then unbalanced magnetic pull occurs. The phenomenon can be described as an imbalance of the radial and tangential forces acting on the rotor or stator surface such that a net radial force is developed. This can result in vibration and noise, and increase the possibility of the stator and rotor contact. Therefore, real-time monitoring of rotor eccentricity is essential in order to prevent serious damage to stator and rotor windings.

Rotor eccentricity faults occur when airgap between the stator and rotor is non-uniform. This non-uniformity can occur in three different forms known as: static eccentricity (SE), deviating stator axis from both rotational and rotor axis, dynamic eccentricity (DE), displacing rotor axis from both

stator and rotational axis, and a combination of both SE and DE called mixed eccentricity (ME), deviating rotor centre, stator centre and the centre of rotation from each other [15].

3.2.1 | Static eccentricity condition

In the presence of a SE fault, the permeance function of the airgap can be modelled as [15]:

$$P = P_0 + P_1 \cos \theta_s \tag{16}$$

The PW airgap flux in stator reference frame and under SE fault condition is obtained from Equation (6) when the constant permeance, P_0 , is substituted using Equation (16).

$$\begin{aligned} \phi_{p,SE}(t, \theta_s) = & \widehat{F}_p P_0 \cos(\omega_p t - p_p \theta_s) + \\ & \frac{\widehat{F}_p P_1}{2} \left\{ \begin{aligned} & \cos \omega_p t - (p_p - 1) \theta_s + \\ & \cos \omega_p t - (p_p + 1) \theta_s \end{aligned} \right\} \end{aligned} \tag{17}$$

Following the same analytical derivation presented from Equations (9) to (12) for healthy condition, the rotor airgap flux in stator reference frame and under SE condition can be written as:

$$\begin{aligned} \phi_{rp,SE}(t, \theta_s) = & \widehat{F}_{rp}(\omega_r) \frac{P_0 P_1}{2} \sin \left(\left(1 \pm k \frac{N_n}{p_p} (1 - S_p) \right) \omega_p t - \right. \\ & \left. (p_p + 1 \pm k N_n) \theta_s \right) + \\ & \widehat{F}'_{rp}(\omega_r) \frac{P_0 P_1}{2} \sin \left(\left(1 \pm k \frac{N_n}{p_p} (1 - S_p) \right) \omega_p t \right. \\ & \left. - (p_p - 1 \pm k N_n) \theta_s \right) + \\ & \widehat{F}''_{rp}(\omega_r) \frac{P_1^2}{4} \sin \left(\left(1 \pm k \frac{N_n}{p_p} (1 - S_p) \right) \omega_p t \right. \\ & \left. - (p_p + 2 \pm k N_n) \theta_s \right) + \\ & \widehat{F}'''_{rp}(\omega_r) \frac{P_1^2}{4} \sin \left(\left(1 \pm k \frac{N_n}{p_p} (1 - S_p) \right) \omega_p t \right. \\ & \left. - (p_p - 2 \pm k N_n) \theta_s \right) \end{aligned} \tag{18}$$

where \widehat{F}_{rp} , \widehat{F}'_{rp} , \widehat{F}''_{rp} , and \widehat{F}'''_{rp} are the magnitudes of the rotor magnetic flux components, which are functions of ω_r . Using Equation (18), the PW current time harmonic frequencies induced by NRSB components at SE fault condition can be obtained from:

$$\left\{ \begin{aligned} f_{SE(k)} &= \left(1 + k \frac{N_n}{p_p} (1 - S_p) \right) f_p \\ & \vee \left\{ \begin{aligned} & |p_p \pm 1 + k N_n| \in |H_p| \\ & |p_p \pm 2 + k N_n| \in |H_p| \end{aligned} \right. \\ f_{SE(k)} &= \left(1 - k \frac{N_n}{p_p} (1 - S_p) \right) f_p \\ & \vee \left\{ \begin{aligned} & |p_p \pm 1 - k N_n| \in |H_p| \\ & |p_p \pm 2 - k N_n| \in |H_p| \end{aligned} \right. \end{aligned} \right. , k = 0, 1, 2, \dots \tag{19}$$

where $f_{SE(k)}$ is the frequency of k -th NRSB harmonic component order in Hz. These harmonic frequencies are used as SE fault indices in Section 4.

3.2.2 | Dynamic eccentricity condition

When DE fault exists, the airgap permeance function is expressed as [15]:

$$P \approx P_0 + P_2 \cos(\theta_s - \omega_r t) \tag{20}$$

The rotor airgap flux with respect to stator reference frame and under DE fault condition can be obtained by following the analytical derivation presented in Section 3.1 and using Equation (20), for representing the airgap permeance.

$$\begin{aligned}
\phi_{rp,DE}(t, \theta_s) = & \\
\widehat{F}_{rp}(\omega_r) \frac{P_0 P_2}{2} \sin \left(\left(1 + (1 \pm kN_n) \frac{(1-s_p)}{p_p} \right) \omega_p t - \right. & \\
& \left. (p_p + 1 \pm kN_n) \theta_s \right) + & \\
\widehat{F}_{rp}(\omega_r) \frac{P_0 P_2}{2} \sin \left(\left(1 + (-1 \pm kN_n) \frac{(1-s_p)}{p_p} \right) \omega_p t - \right. & \\
& \left. (p_p - 1 \pm kN_n) \theta_s \right) + & \\
\widehat{F}'_{rp}(\omega_r) \frac{P_2^2}{2} \sin \left(\left(1 + (2 \pm kN_n) \frac{(1-s_p)}{p_p} \right) \omega_p t - \right. & \\
& \left. (p_p + 2 \pm kN_n) \theta_s \right) + & \\
\widehat{F}'_{rp}(\omega_r) \frac{P_2^2}{2} \sin \left(\left(1 + (-2 \pm kN_n) \frac{(1-s_p)}{p_p} \right) \omega_p t - \right. & \\
& \left. (p_p - 2 \pm kN_n) \theta_s \right) & \\
\end{aligned} \quad (21)$$

Using Equation (21), the PW current time harmonic frequencies induced by NRSB components at the DE fault condition can be obtained:

$$\left\{ \begin{array}{l}
f_{DE(k)} = \left(1 + (\pm 1 + kN_n) \frac{(1-s_p)}{p_p} \right) f_p \\
\quad \forall |p_p \pm 1 + kN_n| \in |H_p| \\
f_{DE(k)} = \left(1 + (\pm 1 - kN_n) \frac{(1-s_p)}{p_p} \right) f_p \\
\quad \forall |p_p \pm 1 - kN_n| \in |H_p| \\
f_{DE(k)} = \left(1 + (\pm 2 + kN_n) \frac{(1-s_p)}{p_p} \right) f_p \\
\quad \forall |p_p \pm 2 + kN_n| \in |H_p| \\
f_{DE(k)} = \left(1 + (\pm 2 - kN_n) \frac{(1-s_p)}{p_p} \right) f_p \\
\quad \forall |p_p \pm 2 - kN_n| \in |H_p|
\end{array} \right. , k = 0, 1, 2, \dots \quad (22)$$

where $f_{DE(k)}$ is the frequency of k -th NRSB harmonic component in Hz. These signature frequencies are used as DE fault indices in Section 4.

3.2.3 | Mixed eccentricity condition

The ME fault condition occurs when a combination of static and dynamic eccentricity is present. The airgap permeance function at this situation can be expressed as [15]:

$$P \approx P_0 + P_1 \cos \theta_s + P_2 \cos(\theta_s - \omega_r t) \quad (23)$$

Following the approach presented in Equations (6)–(14), the rotor airgap flux with respect to the stator reference frame and under the ME fault condition can be expressed as:

$$\begin{aligned}
\phi_{rp,ME}(t, \theta_s) = & \\
\widehat{F}_{rp}(\omega_r) \frac{P_1 P_2}{2} \sin \left(\left(1 + (1 \pm kN_n) \frac{(1-s_p)}{p_p} \right) \omega_p t - \right. & \\
& \left. (p_p + 2 \pm kN_n) \theta_s \right) + & \\
\widehat{F}'_{rp}(\omega_r) \frac{P_1 P_2}{2} \sin \left(\left(1 + (-1 \pm kN_n) \frac{(1-s_p)}{p_p} \right) \omega_p t - \right. & \\
& \left. (p_p - 2 \pm kN_n) \theta_s \right) + & \\
\widehat{F}'_{rp}(\omega_r) \frac{P_1 P_2}{2} \sin \left(\left(1 + (1 \pm kN_n) \frac{(1-s_p)}{p_p} \right) \omega_p t - \right. & \\
& \left. (p_p \pm kN_n) \theta_s \right) + & \\
\widehat{F}_{rp}(\omega_r) \frac{P_1 P_2}{2} \sin \left(\left(1 + (-1 \pm kN_n) \frac{(1-s_p)}{p_p} \right) \omega_p t - \right. & \\
& \left. (p_p \pm kN_n) \theta_s \right) & \\
\end{aligned} \quad (24)$$

Using Equation (24), the PW current time harmonic frequencies induced by NRSB components at the ME fault condition can be obtained by:

$$\left\{ \begin{array}{l}
f_{ME(k)} = \left(1 + (\pm 1 + kN_n) \frac{(1-s_p)}{p_p} \right) f_p \\
\quad \forall \left\{ \begin{array}{l} |p_p \pm 2 + kN_n| \in |H_p| \\ |p_p + kN_n| \in |H_p| \end{array} \right. \\
f_{ME(k)} = \left(1 + (\pm 1 - kN_n) \frac{(1-s_p)}{p_p} \right) f_p \\
\quad \forall \left\{ \begin{array}{l} |p_p \pm 2 - kN_n| \in |H_p| \\ |p_p - kN_n| \in |H_p| \end{array} \right. \\
\end{array} \right. , k = 0, 1, 2, \dots \quad (25)$$

where $f_{ME(k)}$ is the frequency of $k - th$ NRSH harmonic component in Hz . These signature frequencies are therefore considered as ME fault indices. Consequently, by applying Equations (15), (19), (22) and (25), the signature frequencies associated with the healthy and different eccentricity fault conditions can be detected in a BDFIM. It will be shown in the next section and by using the winding function method and FE analysis that the above signature frequencies derived analytically will also be seen in the PW current spectrum of the prototype BDFIM. It should be noted that the above equations are dependent to the rotor speed due to the presence of slip terms (s_p). This means that the proposed method can be applied to any steady state condition with constant rotor speed, but the signature frequencies will be different at different rotor speeds.

4 | ASSESSMENT OF THE PROPOSED FAULT DETECTION METHOD

In order to assess the validity of the proposed fault detection method, a D180 BDFIM, described in Table 1, is modelled under both healthy and eccentricity fault conditions using the winding function method and FE analysis in the synchronous mode of operation with the operating conditions presented in Table 2. Although, the models are developed for the mentioned operating conditions in Table 2, the proposed method in Section 3 is a generic technique and can be used at any operating conditions. The winding function method has previously been developed and verified by the authors for the BDFIM, for example in [19]. The PW space harmonic orders are calculated using Equation (5) and presented in Table 3.

4.1 | Healthy condition

Under healthy conditions and according to Equation (15), it can be shown that the NRSH components for even values of k have the same harmonic orders with the PW space harmonics given in Table 3. Hence, the corresponding frequencies to these k values are expected to be seen in the stator PW current spectrum. The NRSH component orders and the correspondent frequencies within the PW current are obtained using Equation (15) for healthy condition and presented in Table 4. Figure 6 shows the PW current spectrum in the synchronous mode and under healthy condition obtained by winding

TABLE 3 The PW space harmonic orders obtained from Equation (5)

g	0	1	2	3	4
$ H_p = (1 + 6g)p_p $	2	14	26	38	50
$ H_p = (1 - 6g)p_p $	2	10	22	34	46

TABLE 4 The harmonic component orders and frequencies induced in the PW current in a healthy condition as predicted by Equation (15)

k	0	2	4	6
$ p_p + kN_n $	2	14	26	38
$ (1 + k\frac{N_n}{p_p}(1 - s_p))f_p Hz$	50	158	266	374
$ p_p - kN_n $	2	10	22	34
$ (1 - k\frac{N_n}{p_p}(1 - s_p))f_p Hz$	50	58	166	274

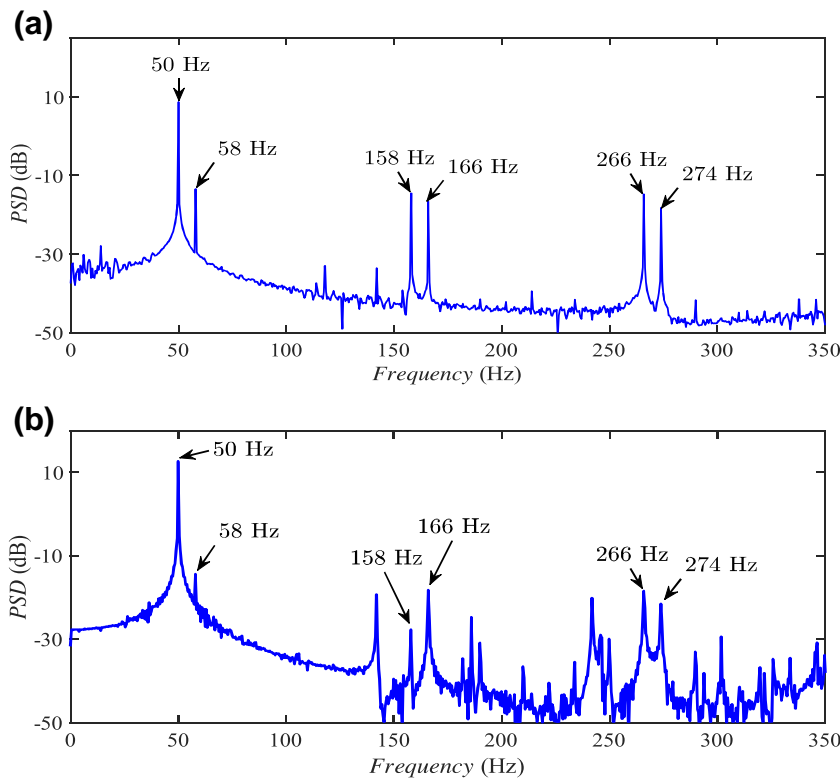


FIGURE 6 The PW current spectrum in healthy condition obtained from (a) Winding function approach (b) FE analysis

function approach and FE analysis. Based on Table 4, a set of frequencies $\{50, 58, 158, 166, 266, 274\}$ Hz are expected to be induced in the PW current spectrum. These harmonic frequencies are also seen in Figure 6 validating the proposed analytical method for healthy condition.

4.2 | Static eccentricity fault

Under SE fault condition and based on Equation (19), the NRSH components with the orders of $p_p + 2 \pm kN_n$ given that k is an odd integer, have the same harmonic orders with PW space harmonics presented in Table 3. These harmonic components are hence expected to be seen in PW current spectrum. The corresponding frequencies of harmonic components obtained from Equation (19) are shown in Table 5.

The PW currents for the prototype machine are obtained under 20% SE fault using the winding function method and FE analysis and their frequency spectra are shown in Figure 7.

TABLE 5 The harmonic component orders and frequencies induced in PW current in SE fault condition predicted by Equation (19)

k	1	3	5	7
$ p_p + 2 + kN_n $	10	22	34	46
$ (1 + k\frac{N_n}{p_p}(1 - s_p))f_p $ Hz	104	212	320	428
$ p_p + 2 - kN_n $	2	14	26	38
$ (1 - k\frac{N_n}{p_p}(1 - s_p))f_p $ Hz	4	112	220	328

As can be seen, additional harmonic frequencies, $\{4, 104, 112, 212, 220, 320, 328\}$ Hz, are induced in the PW currents compared to the healthy condition. These frequencies are also predicted in Table 5, which confirms the validity of the proposed analytical derivation of signature frequencies associated to the SE faults. The signature frequencies obtained from Equation (19) can therefore be used as fault indices for diagnosis of SE faults in BDFIMs.

4.3 | Dynamic eccentricity fault

According to Equation (22), it can be shown that when a DE fault occurs, the NRSH components with harmonic orders of $p_p + 2 \pm kN_n$, will have the same harmonic orders as PW space harmonics presented in Table 3. Therefore, the associated frequencies with those harmonic components, are expected to be induced in the PW current spectrum. The PW currents of the prototype BDFIM are obtained under DE fault conditions and under 20% of fault intensity using winding function method and FE analysis. The current spectra are shown in Figure 8. It is evident that the harmonic frequencies $\{14, 94, 122, 202, 230, 310, 338\}$ Hz are induced in the PW currents. These frequencies can also be seen in Table 6 obtained from Equation (22) confirming the validity of the analytical derivation of the signature frequencies when DE faults exist. Those signature frequencies can therefore be used as fault indices for diagnosis of DE faults in the BDFIMs.

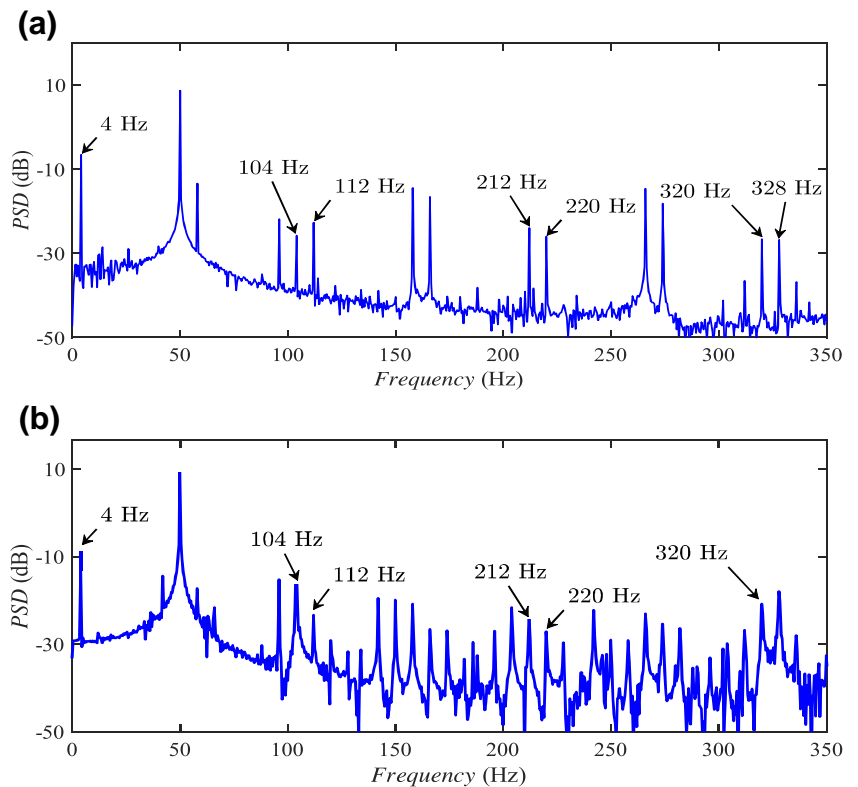


FIGURE 7 The PW current spectrum under 20% SE fault condition obtained from (a) Winding function method (b) FE analysis

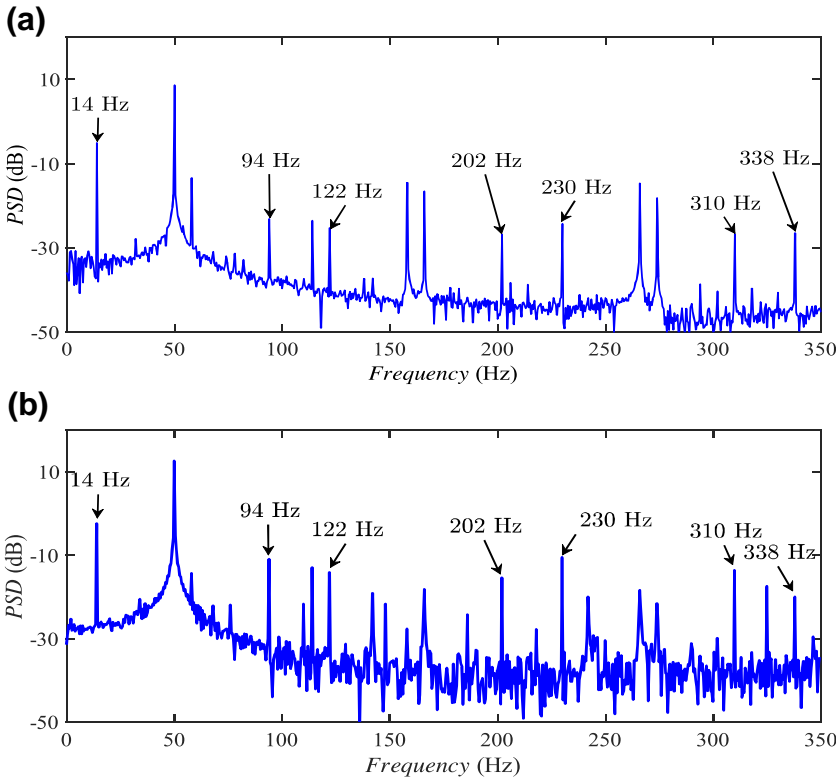


FIGURE 8 The PW current spectrum under 20% DE fault condition obtained from (a) winding function method (b) FE analysis

TABLE 6 The harmonic component orders and frequencies induced in PW current in the DE fault condition predicted by Equation (22)

k	1	3	5
$ p_p + 2 + kN_n $	10	22	34
$ (1 + k\frac{N_n}{p_p}(1 - s_p))f_p $ Hz	122	230	338
$ p_p + 2 - kN_n $	2	14	26
$ (1 - k\frac{N_n}{p_p}(1 - s_p))f_p $ Hz	14	94	202

TABLE 7 The harmonic component orders and frequencies induced in PW current in the ME fault condition predicted by Equation (25)

k	0	2	4	6
$ p_p + kN_n $	2	14	26	38
$ (1 + k\frac{N_n}{p_p}(1 - s_p))f_p $ Hz	41	149	257	365
$ p_p - kN_n $	2	10	22	34
$ (1 - k\frac{N_n}{p_p}(1 - s_p))f_p $ Hz	41	67	175	283

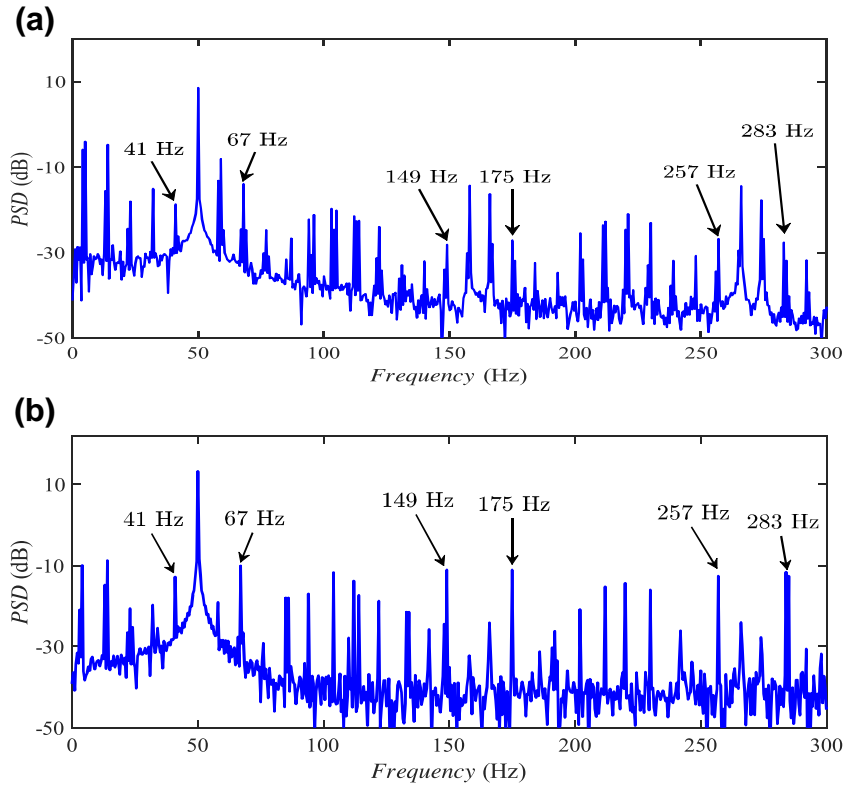
4.4 | Mixed eccentricity fault

It has been shown in Section 3.2.3 that when ME fault occurs, NRSB components with harmonic orders of both $p_p \pm kN_n$ and $p_p + 2 \pm kN_n$ are generated. However, it can be shown that the NRSB frequencies associated with $p_p + 2 \pm kN_n$ harmonic orders are close to SE fault indices; therefore, it is difficult to distinguish the type of eccentricity faults. However, the NRSB frequencies associated with $p_p \pm kN_n$ harmonic orders when k is an even integer, will result in distinct signature frequencies, and hence can be used specifically for ME fault detection purposes. The ME signature frequencies are presented in Table 7. The PW currents are obtained for the prototype machine using winding function method and FE analysis where both SE and DE faults are presented with 20% intensity. The current spectra are shown in Figure 9. As evident, a set of frequency

$\{41, 67, 149, 175, 257, 283\}$ Hz are induced in PW currents. These frequencies are the same as those obtained from Equation (25) for $p_p \pm kN_n$ harmonic orders validating the proposed analytical method for identifying the ME signature frequencies for the BDFIMs.

It should be noted that there are several harmonic components that existed in the PW current obtained from FE analysis which have not been identified as fault indices. These are believed to be induced in the PW current by other harmonic sources such as iron saturation, skin effects in rotor bar current distribution, stator and rotor slotting effects and possible cross coupling of PW and CW through the rotor winding [9]. These effects were automatically taken into account in the FE nonlinear models, whereas they are ignored in the WF method. In [9] an extensive harmonic analysis of the BDFIM was performed and some of the common harmonic sources were identified:

FIGURE 9 The PW current spectrum under the ME fault condition, where 20% SE and 20% DE fault intensity are considered. The currents are obtained from (a) Winding function method (b) FE analysis



- In the nested-loop rotor the cross coupling between the PW and CW is enabled using a single rotor winding at the cost of producing excessive undesirable spatial harmonics with harmonic orders of $P_p \pm kN_n$ and $P_c \pm kN_n$, where k is an integer number.

- Further undesirable harmonics are generated when the rotor teeth are magnetically saturated. Iron saturation also causes additional harmonic order of $3P_p \pm kN_n$ and $3P_c \pm kN_n$ which are superimposed to the airgap magnetic field making the field further distorted.

- In addition, slot harmonic orders of $N_s + P_p/P_c$ and $N_r + P_p/P_c$ related to stator and rotor slots, respectively, are created in the BDFIM magnetic fields, where N_s and N_r are stator and rotor slot numbers, respectively.

The above harmonic orders as well as other unknown sources of harmonics can produce various time harmonics in the stator currents. It is, however, not straightforward to identify the exact time harmonic frequencies were induced in stator currents and hence a comprehensive analytical and numerical study of the BDFM structure and field patterns is required to be carried out.

4.5 | Sensitivity analysis of the fault diagnosis method

A sensitivity analysis of the fault indices was carried out for different types of eccentricity faults and at various fault intensity levels. The fault intensity of 0%, corresponding to

healthy condition, 10%, 20%, 30% and 40% were considered for SE and DE faults and the magnitudes of the fault indices were obtained using FE analysis. The results are shown in dB in Figure 10a,b. In addition, three different combinations of SE and DE fault intensity are considered to assess the sensitivity of the ME fault indices and the results are shown in Figure 10c.

As can be seen, the magnitude of fault indices varies in the range of 20 to 50 dB for all different types and levels of eccentricity. This range of magnitudes is sufficiently large to be used for fault detection purposes [27]. In addition, there are growing trends in the magnitudes of fault indices when fault intensity is increased for different eccentricity types. This confirms the practicality of the proposed fault diagnosis method to be used for a wide range of fault intensity.

Figure 11 shows the amplitude of SE, DE and ME fault indices at various load conditions obtained from winding function method when the machine is operated at synchronous mode of operation. The results confirm that the sensitivity of fault indices to the machine's load variation is negligible and hence the proposed fault detection method can be used for any load condition.

4.6 | Experimental verification

The test bench for the BDFM is shown in Figure 12. The machine is operated in synchronous mode and at rated conditions. The delta connected PW is connected to the grid

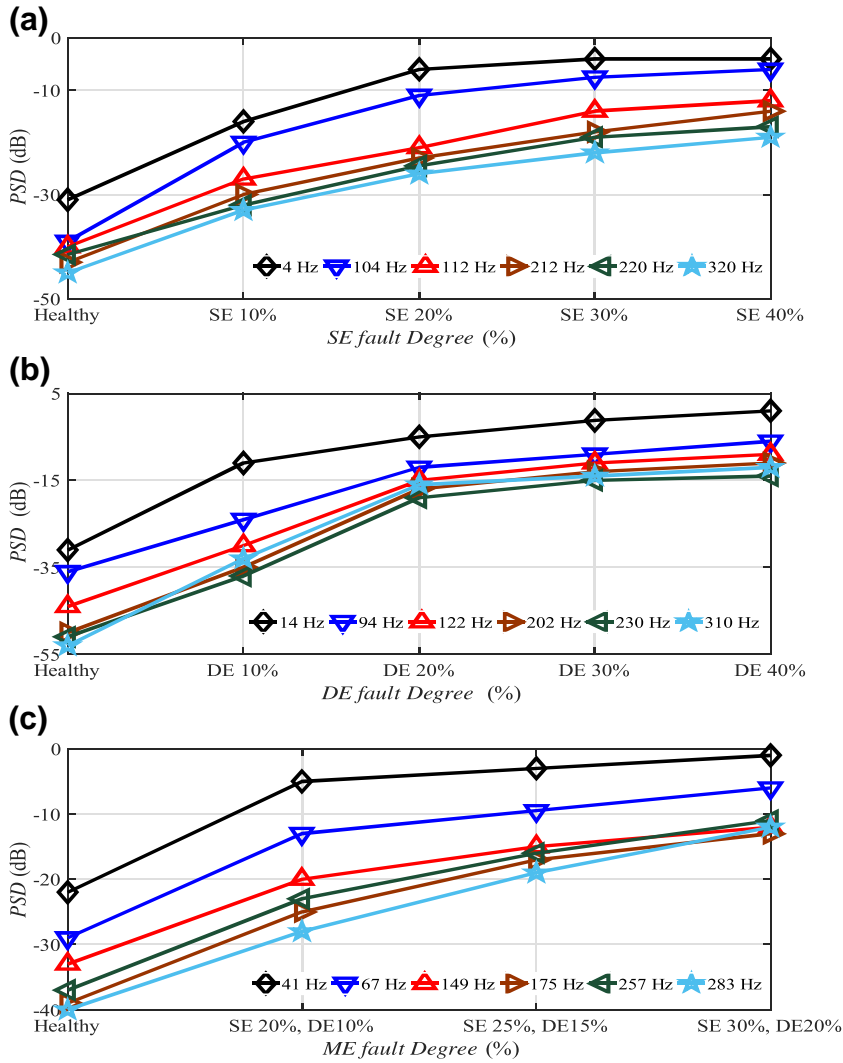


FIGURE 10 Variation of the magnitudes of fault indices with fault intensity for (a) SE fault (b) DE fault (c) ME fault

through a variac and is supplied at 204 V_{rms} , 50 Hz . The CW is also connected in delta and supplied by a unidirectional converter at 50 V_{rms} , 4 Hz . A sinusoidal filter is connected between the converter output and the CW to filter out the harmonic produced by converter's switching frequency. The per-phase resistance values of PW and CW were obtained by DC measurements and are 6.3 Ω and 3.9 Ω , respectively. The voltages and currents of each stator phase are measured by LEM LV 25-p and LEM LTA 100-p transducers, respectively. The control algorithm was implemented in MATLAB Simulink, which receives all the signals stated above and generates PWM signals for the converter. Experimental tests were carried out on the prototype D180 BDFIM described in Section 2. The machine was operated at a synchronous mode where, the PW was supplied at 204 V , 50 Hz and the CW was supplied via an inverter at 50 V , 4 Hz . The rotor synchronous speed was therefore set at 540 rpm based on Equation (2). The airgap length at different locations around the rotor was carefully measured.

The design value of the airgap length for the machine is 0.9 mm , while the biggest airgap length measured around the rotor circumference was 0.97 mm , showing an approximate 8% of static eccentricity. This is mainly due to manufacturing tolerances and the non-ideal structure of the couplings. The PW current was measured, and the current spectrum is shown in Figure 9. The signature frequencies {4, 104, 112, 212, 220, 320} Hz predicted by the proposed fault detection method and using Equation (18) for the case of static eccentricity and the above operating conditions can also be seen in the PW current of Figure 13, confirming the validity of the proposed method in detecting eccentricity faults.

It should be noted that the experimental results presented in this study only validate the ability of fault detection technique in detecting SE faults. Therefore, future work may include assessment of the proposed technique in detecting DE and ME faults by emulating those faults in the BDFIM experimentally.

FIGURE 11 Amplitude of NRSH frequency with respect to the load variation in synchronous mode Under (a) 20% SE fault condition; (b) 20% DE fault condition (c) ME fault condition (20% SE and 20% DE)

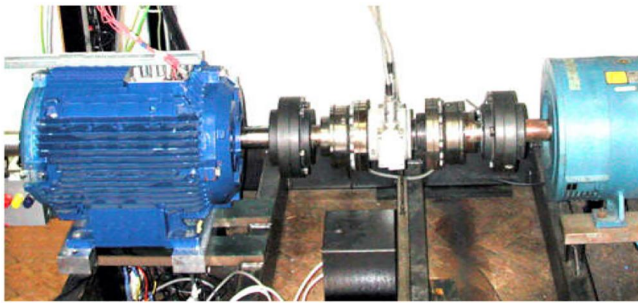
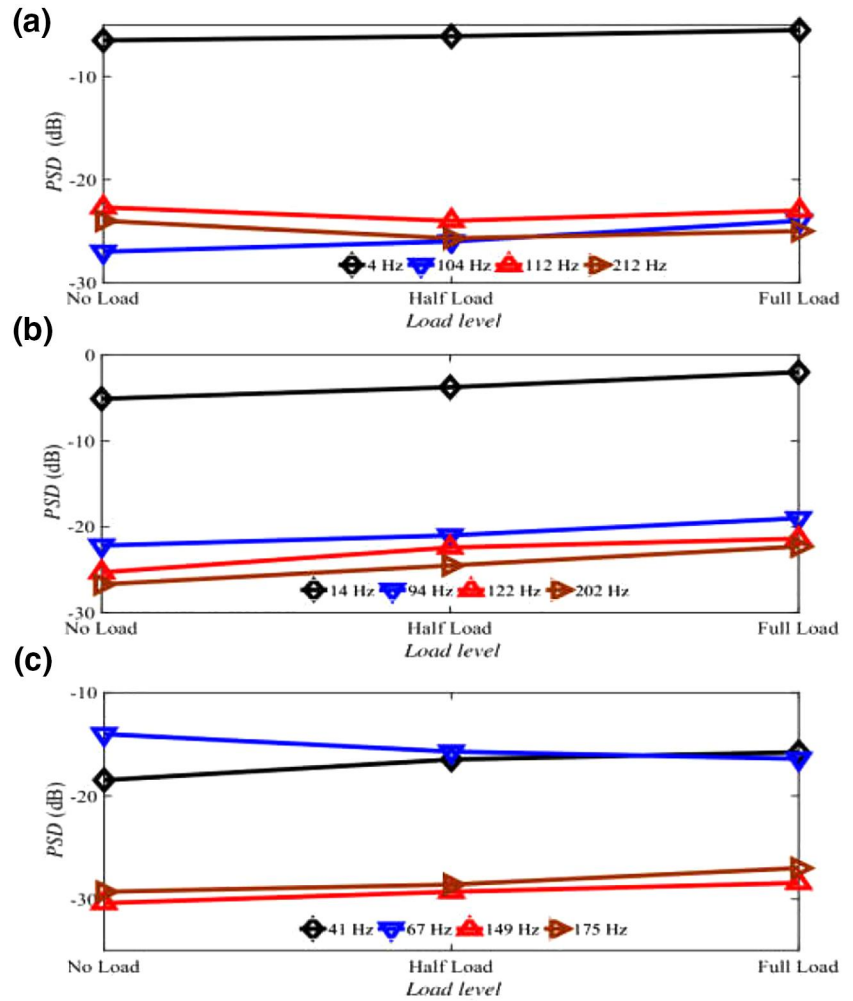


FIGURE 12 D180 prototype BDFIM (left) on the test rig with torque transducer and DC load machine (right)

5 | CONCLUSIONS

This article proposes a novel MCSA-based fault detection method to detect different types of rotor eccentricity faults in the BDFIM. In the proposed method, the airgap magnetic field has been determined analytically under healthy conditions

and different types of rotor eccentricity faults are considered. Rotor harmonic analysis has then been performed for a BDFIM with a nested-loop rotor configuration to obtain the time harmonic frequencies induced in the stator PW current under healthy and faulty conditions. The signature frequencies associated with each eccentricity type have been identified as fault indices.

The proposed fault diagnosis method has been verified using an analytical winding function method as well as a numerical FE analysis of an experimental D180 BDFIM. The machine has been modelled under healthy and different rotor eccentricity conditions, and the PW currents have been obtained. It has been shown that the same signature frequencies predicted by the fault detection technique are also induced in the PW current confirming the practicality of the proposed technique in determining the eccentricity fault indices. Furthermore, a sensitivity analysis of fault indices at different fault intensity levels has been carried out for various eccentricity types concluding that fault indices can be used for a wide range of eccentricity fault intensity in the BDFIM [28].

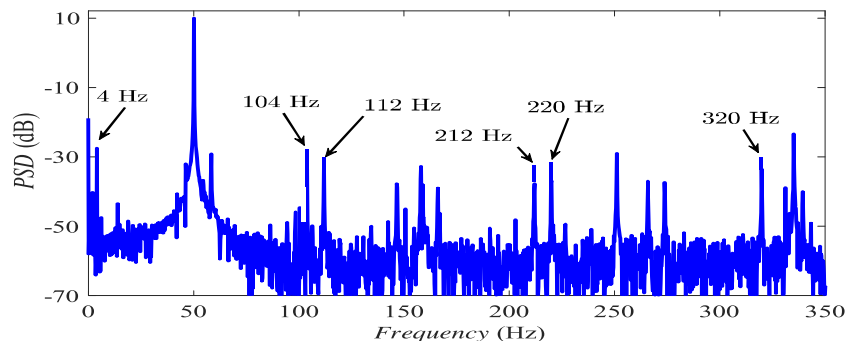


FIGURE 13 The power winding current spectrum obtained from experimental tests on a prototype D180 BDFIM

ORCID

Mojtaba Afshar  <https://orcid.org/0000-0002-6173-0440>

REFERENCES

1. Strous, T., Polinder, H., Ferreira, J.: Brushless doubly fed induction machines for wind turbines: developments and research challenges. *IET Electric. Power Appl.* 11, 991–1000 (2017)
2. Roberts, P.: A study of brushless doubly-fed (induction) machines, PhD thesis. University of Cambridge (2004)
3. Gorti, B., Alexander, G., Spee, R.: A novel, cost-effective stand-alone generator system. *Proceedings of IEEE. AFRICON96*, vol. 2, pp. 626–631 (1996)
4. Wallace, A.K., Spee, R., Lauw, H.K.: The potential of brushless doubly-fed machines for adjustable speed drives. *Annual Technic Conference on Pulp and Paper Industry*, vol. 1, pp. 45–50 (1990)
5. Xiong, F., Wang, X.: Design and performance analysis of a brushless doubly-fed machine for stand-alone ship shaft generator systems. *Int. Conf. on Electrical and Control Engineering*. 53, 2114–2117 (2011)
6. Cheng, M., et al.: Emerging multiport electrical machines and systems: past developments, current challenges, and future prospects. *IEEE Trans. Ind. Electron.* 65, 5422–5435 (2017)
7. Wang, X., McMahon, R., Tavner, P.J.: Design of the brushless doubly fed (induction) machine. *IEEE Int. Electric Machines and Drives Conf.* 2, 1508–1513 (2007)
8. Liu, H., Xu, L.: Design and performance analysis of a doubly excited brushless machine for wind power generator application. *IEEE Int. Symposium on Power Electronics for Distributed Generation Systems*. 52, 597–601 (2010)
9. Gorginpour, H., Jandaghi, B., Oraee, H.: A novel rotor configuration for brushless doubly-fed induction generators. *IET Electr. Power Appl.* 7, 106–115 (2013)
10. Runcos, F., et al.: Performance and vibration analysis of a 75 kw brushless doublefed induction generator prototype. *IEEE Industry Applications Conf. Forty-First IAS Annual Meeting*. 5, 2395–2402 (2006)
11. Liu, H., Xu, L.: Design and performance analysis of a doubly excited brushless machine for wind power generator application. *IEE Int. Symposium on Power Electronics for Distributed Generation Systems*. 4, 597–601 (2010)
12. Abdi, E., et al.: Performance analysis and testing of a 250 kw medium-speed brushless doubly-fed induction generator. *IET Renew. Power Gener.* 7, 631–638 (2013)
13. Nandi, S., Toliyat, H.A., Li, X.: Condition monitoring and fault diagnosis of electrical motors: a review. *IEEE Trans. Energy Conv.* 20, 719–729 (2005)
14. Daniar, A., Nasiri-Gheidari, Z., Tootoonchian, F.: Position error calculation of linear resolver under mechanical fault conditions. *IET Sci. Meas. Technol.* 11, 948–954 (2017)
15. Nandi, S., Ahmed, S., Toliyat, H.A.: Detection of rotor slot and other eccentricity related harmonics in a three phase induction motor with different rotor cages. *IEEE Trans. Energy Conv.* 16, 253–260 (2001)
16. Ebrahimi, B.M., Faiz, J., Roshtkhari, M.J.: Static-, dynamic-, and mixed-eccentricity fault diagnoses in permanent-magnet synchronous motors. *IEEE Trans. Ind. Electron.* 56, 4727–4739 (2009)
17. Afshar, M., et al.: Stator short-circuit fault detection and location methods for brushless DFIMs using nested-loop rotor slot harmonics. *IEEE Trans. Power Electron.* (2019)
18. Afshar, M., et al.: A new stator winding inter-turn short circuit fault detection method for brushless doubly fed induction machine. In: *ISIE 29th Annual Conf. of the IEEE Int. Symposium on Industrial Electronic (2020)*
19. Afshar, M., et al.: Static eccentricity fault detection in brushless doubly-fed induction machines based on motor current signature analysis. *IECON 45th Annual Conf. of the IEEE Industrial Electronics Society*, vol. 1, pp. 1369–1374 (2019)
20. Logan, T., McMahon, R., Seffen, K.: Noise and vibration in brushless doubly fed machine and brushless doubly fed reluctance machine. *IET Electric. Power App.* 8, 50–59 (2014)
21. Zhang, F.G., Wang, F.X., Wang, Z.: Comparative experiment study on the performance of doubly-fed brushless machine with different rotor structures. *Proceedings of the CSEE*, vol. 4, pp. 846–850 (2002)
22. Abdi, S., Abdi, E., McMahon, R.: A study of unbalanced magnetic pull in brushless doubly fed machines. *IEEE Trans. Energy Conv.* 30, 1218–1227 (2015)
23. Abdi, S., et al.: Experimental analysis of noise and vibration for large brushless doubly fed machines. *J. Eng.* 13, 724–728 (2017)
24. Sharifi, V., Ebrahimi, M.: Detection of stator winding faults in induction motors using three-phase current monitoring. *ISA Trans.* 50, 14–20 (2011)
25. Choqueuse, R., Benbouzid, M.E.H.: Current frequency spectral subtraction and its contribution to induction machines bearings condition monitoring. *IEEE Trans. Energy Conv.* 28, 135–144 (2013)
26. Penman, J., et al.: Detection and location of interturn short circuits in the stator windings of operating motors. *IEEE Trans Energy Conv.* 9, 652–657 (1994)
27. Blazquez, F., et al.: Characterization of the rotor magnetic field in a brushless doubly-fed induction machine. *IEEE Trans. Energy Conv.* 24, 599–607 (2009)
28. Gyftakis, K.N., Kappatou, J.C.: A novel and effective method of static eccentricity diagnosis in three-phase PSH induction motors. *IEEE Trans. Energy Conv.* 28, 405–412 (2013)

How to cite this article: Afshar M, Abdi S, Oraee A, Ebrahimi M, McMahon R. Eccentricity fault detection in brushless doubly fed induction machines. *IET Electr. Power Appl.* 2021;15:916–930. <https://doi.org/10.1049/elp2.12060>